Fourier Accelerated Multistatic Imaging: A Fast Reconstruction Algorithm for Multiple-Input-Multiple-Output Radar Imaging

DANIEL L. MARKS, OKAN YURDUSEVEN, (Senior Member, IEEE), AND DAVID R. SMITH, (Member, IEEE)

Center for Metamaterials and Integrated Plasmonics, Department of Electrical and Computer Engineering, Duke University, Durham, NC 27708, USA

Corresponding author: D. L. Marks (daniel.marks@duke.edu)

ABSTRACT Multiple-input-multiple-output (MIMO) radar image processing presents problems difficult to address by modifying conventional monostatic radar methods as Fourier range migration. When the distance between the transmitter and receiver is comparable to the target size, the single phase center approximation is not accurate. Furthermore, if the antenna radiation pattern significantly deviates from a spherical wave, the symmetries assumed in most range migration techniques are violated. We present a rapid Fourier-based MIMO reconstruction called Fourier accelerated multistatic imaging (FAMI) suitable for massively parallel computation that accounts for frequency-dependent radiation patterns, does not require the single phase center approximation, and is able to dynamically adapt to different target support volume shapes. FAMI is especially suitable for frequency-diversity antenna systems that use spectrally modulated coded spatial radiation patterns.

INDEX TERMS MIMO, radar, imaging, Fourier, multistatic, reconstruction, GPGPU.

I. INTRODUCTION

Multiple-input multiple-output (MIMO) radar [1]–[3] have become more attractive recently due to advances in electronic integration, signal processing, and antenna designs. Real-time imaging applications such as vehicle navigation, security checkpoint scanning, aerial surveillance, and robotic motion planning benefit from the rapid data acquisition of MIMO radars. However, MIMO radar imaging, especially in indoor environments for which the size of the objects is comparable to the size of the radar system, presents special challenges that are rarely encountered by large-scale radar systems. As the cross-range resolution depends on the angle the antenna array subtends to the target, transmitters and receivers may be located on nearly opposite sides of the target in order to achieve a resolution limited by the illumination wavelength. Furthermore, emerging methods of radar imaging such as frequency diversity [4] use spectrally coded antenna radiation patterns to determine the structure of the target. Standard methods of radar image formation, such as the range migration algorithm, often assume simple, short dipole-like radiation patterns of the antennas rather than complex radiation patterns, and furthermore use a single phase-center approximation where measurements between a distantly located transmitter and receiver are approximated as if these measurements were recorded by a single transceiver placed between the transmitter and receiver. While for a single moving platform, such as an airplane or satellite, these assumptions may be sufficiently accurate, for MIMO radars these assumptions may produce significant error that prevents satisfactory image formation. While image reconstruction algorithms such as backpropagation and direct algebraic inversion can account for these effects, these are often too slow for real-time imaging. We propose and demonstrate a method of MIMO radar inversion called Fourier Accelerated Multistatic Imaging (FAMI) that does not require a single phase-center approximation, accounts for complex antenna radiation patterns, and produces three-dimensional reconstructions of targets, designed specifically for implementation with highly parallel processors such as general-purpose graphics processing units (GPGPUs) so that the inversion may be suitably rapid for real-time imaging on mobile platforms with modest computational capability.

In order to understand why another method of radar inversion is desirable, we examine existing radar inversion algorithms. Broadly speaking, these can be grouped into two categories, algebraic methods [5] and Fourier-based

methods [6]–[9]. Algebraic methods use a model of electromagnetic scattering that is very general and can account for nonuniform and distributed layouts of transmitter and receiver antennas as well as variations in the radiation patterns of antennas. The simplest algebraic approach is imaging by backpropagation, where the received signals are summed backwards along the paths from the receiver to the source coherently. Formally, if the linear operation relating the measurements to the target susceptibility is called the forward operator, backpropagation is applying the adjoint of the forward operator to the measurements. This may be further refined by using the forward and adjoint operators to implement a true least-squares or other regularized inverse problem, typically in an iterative reconstruction algorithm [10]. While very general, this method can be quite slow and unsuitable for real-time imaging, and is therefore reserved for situations for which the best possible reconstruction quality must be achieved regardless of the effort. Algebraic methods can be optimized and accelerated for graphics processing hardware, as was achieved on the Virtualizer simulation framework [11], [12], but because of their generality, algebraic methods may fail to take advantage of approximations or shortcuts that could speed the computation without causing appreciable image degradation.

For more rapid computational image formation, methods such as the Fourier range-migration algorithm are used. These methods are extremely fast and efficient. Fourier migration exploits the fact that most radar antennas produce an isotropic-like radiation pattern similar to a short dipole, and that the measurements are taken by a collocated, monostatic transceiver that is sampled at regular spatial and spectral intervals. Because of the high symmetry of this situation, Fourier integrals may be used to model diffraction, and therefore fast Fourier transform methods may be used to accelerate the inversion process. Unfortunately, this method becomes increasingly hard to adapt when these symmetries are broken, for example, when the measurements are no longer monostatic or the antennas are no longer isotropic. While a nearly co-located transmitter and receiver can be approximated as being a monostatic transceiver positioned between the two, i.e. the single-phase center or pseudomonostatic approximation [13], [14], for large baseline MIMO arrays this approximation is poor, and excluding measurements between distant transmitters and receivers limits the potential reconstruction quality. However, corrections may be made to the single-phase center approximation for small displacements between transmitters and receivers [15]–[18] to allow a monostatic-like solution to be used. A further method modifies the Stolt interpolation step [19] to account for the separation in a bistatic baseline. Compressed sensing methods [20], [21] employing basis pursuit to identify point scatterers as well several other explorations of compressed sensing applied to radar [22]–[25] can be accelerated using FAMI, as many of these methods can use alternate methods of implementing the forward and adjoint operator, and compressed sensing methods help utilize available information about object sparsity or support to further enhance the image. Ideally, an algorithm should take advantage of all available data and not itself limit the utility of the data. Therefore an algorithm is desirable that could allow flexible placement of transmit and receive antennas, as well as choices of their radiation patterns, while still achieving the best computational performance given the reduced symmetry of the problem.

Another consideration for a successful radar algorithm is its suitability for implementation in parallel processing hardware. As the limitations of central processing unit (CPU) based computation have become apparent, other models of computing have become more prominent such as that of the parallel processing GPGPU. Other synthetic aperture radar algorithms have already successfully been implemented on GPGPUs, including backprojection methods [26], [27], Kirchoff migration [28], range-Doppler methods [29], Fourier range migration [30], and range cell migration correction [31]–[33]. This relatively new model of computation has been highly successful at speeding image formation algorithms as well as graphics processing, but have its own limitations that must be considered. In particular, while GPGPUs have many compute units that perform hundreds or thousands of floating point computations simultaneously, these compute units usually share a common global memory. The latency and contention for accessing the common memory is a primary consideration when designing an algorithm to be executed rapidly on a GPGPU. GPGPUs are equipped with memory caches to mitigate the latency and contention problems, so that designing the algorithm to use cached memory rather than shared global memory is crucial to achieving the best performance. Because these caches are frequently designed to accelerate the types of memory access patterns that would occur during graphics processing, an algorithm that uses similar access patterns better avails itself of the cache. More generally, an algorithm suited to parallel processing minimizes the interdependencies between computations so that calculations may be parceled out to many processing units, minimizing the time that processing units are idle waiting for the results of another computation. It is with these goals in mind that a new radar processing algorithm was designed.

In order to simplify the general problem of MIMO radar image formation, a couple of assumptions were made. While the positions of the transmitter and receiver antennas are not constrained, the entire occupied volume of the target must be in the radiation zone (far-field) of each antenna individually. It is not required for the occupied volume to be in the far-field of the antennas considered collectively, so this assumption applies in many practical situations. In practice this means for all antennas, if d is the extent of an antenna, λ is the wavelength, and z is the range to the target from an antenna, then $z > 2d^2/\lambda$. Furthermore, a surface approximately aligned to the cross-range directions through the occupied volume of the target must be known. Ideally, this surface coincides with the scattering front surface of the object. This may appear to be a serious limitation, but such information may often

be obtained by other means, such as structured illumination position sensors or ultrasonic transducers. Alternatively, a combination of antennas may be used, some of which have simple radiation patterns that may be used to locate this surface using conventional ranging techniques, and others which have complex radiation patterns to provide more information about the structure of scatterers on this surface. This surface serves as the focus surface of the image formation, so that point scatterers on this surface are imaged without defocus, and further away from this surface the point scatterers are more defocused. Points that are within the Rayleigh range Δz of the surface for a given antenna array achieve the best focus. For an antenna array with a total baseline length b, $\Delta z = z^2 \lambda / b^2$. In the subsequent analysis of FAMI, a diffraction integral is approximated by the method of stationary phase, and the points on the surface are the stationary points at which the diffraction integral is evaluated and the most accurate approximation is obtained.

One of the main benefits of FAMI is that is allows for much of the flexibility of the algebraic inversion methods, that is, nearly arbitrarily placed antennas with complex radiation patterns, but utilizes Fourier transform techniques that enable rapid computation. It may be considered a hybrid of algebraic techniques and Fourier range migration. The primary operation of the Fourier range-migration method that achieves efficient computation is Stolt interpolation, which is the resampling or discrete change-of-variables operation in the Fourier domain. FAMI uses the same approach to achieve efficient computation, but adaptively changes the interpolation function to suit the geometrical configuration of the transmit and receive antennas relative to the target volume. In fact, when the target volume is in the far-field of the entire antenna array baseline and not just the antennas individually, FAMI simplifies to the standard radar ranging image formation method, so that one of the main advantages of FAMI is that interactions between the antennas in the near field of the baseline are accounted for properly. Because of this, FAMI produces correct results whether or not the target is remote or even between antenna pairs, as long as the target remains in the far-field of the antennas individually.

The motivation to develop FAMI is stimulated by two developments: metamaterial structures that have complex frequency responses, and the construction of antennas with complex radiation patterns based on metamaterials [34], [35]. These antennas produce highly structured radiation patterns, unlike the simple ordinary diverging beam of most SAR systems, that change rapidly with frequency. Frequency diversity [4] imagers takes advantage of these frequency-dependent structured radiation patterns to form images of remote objects, replacing mechanically scanned antennas with faster electronically swept frequency scanning. However, as these radiation patterns are complex, methods that assume high symmetry such as Fourier methods are generally not useful for these imagers, and the algebraic techniques tend to be computationally burdensome. FAMI was developed in part to make frequency diversity imaging more practical and

suitable for real-time computation. As one of the intended applications of frequency diversity imagers is checkpoint security scanners, the reconstruction time must be sufficiently fast as to not cause any delays in screening. As frequency diversity and FAMI acquires data and reconstructs images at near video rates, passengers may be screened more quickly.

The paper is organized into several sections. Section II formally specifies the problem to be solved and derives a mathematical solution for the image formation problem. The basic implementation of this solution based on the derivation is discussed in Section III. Section IV explains how FAMI may advantageously be implemented on GPGPU hardware, with the mathematical operations mapped to graphics primitives offered in the GPGPU computing model, and then provides a specific example based on the NVIDIA Corporation(Santa Clara, CA) Compute Unified Device Architecture (CUDA) GPGPU hardware. FAMI is then tested in simulation in section V, where a known algebraic-based method, the Virtualizer, is used to compute synthetic measurements from simulated targets, and these measurements are then used by FAMI to reconstruct the target from the measurements. Finally, in section VI an analysis of the results is performed to offer conclusions about the performance of FAMI and potential further improvements.

II. DERIVATION OF FAMI

To derive FAMI, a scalar approximation is used. It may be generalized to fully three-dimensional vector fields by using the dyadic product of the transmit and receive fields rather than their simple product, a tensor-valued susceptibility of the target, and a vector current density for the antenna sources. However, as these considerations do not change the computation except to add additional degrees of freedom to be acccounted for, a scalar solution is sufficient to derive and demonstrate FAMI. Furthermore, the single scattering (or first-Born) approximation is used to derive the scattering from the target. The limitations of the first Born approximation have been explored [5], [36].
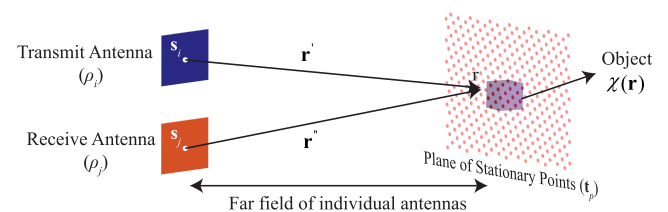
FIGURE 1. A diagram of the geometry of a transmit (blue) and receive (red) antenna, showing the target (a cube), and the surface of stationary points (pink dots). The coordinate **r′** is in the space of the field radiated by the transmit antenna, the coordinate **r″** is in the space of the field radiated by the receive antenna, with **r** being in the space of the target. The transmit and receive antennas have source densities ρ_i and ρ_j respectively.

The MIMO imaging system is defined by a number of transmit and receive antennas and a target contained with a target volume, as shown in Fig. 1. The target is assumed to be nonmagnetic and measurements are unchanged upon

exchange of a transmit and receive antenna. The transmit and receive antennas are indexed by i and j, respectively. The transmit antennas radiates a field $E_i(\mathbf{r}; k)$ into the target volume, and the receive antenna detects a radiated field given by $E_j(\mathbf{r}; k)$, with $\mathbf{r}$ being the coordinate in the target volume, and k being the illumination spatial frequency. The radiation patterns of the antennas are the far fields of the antennas distant from the source. The antenna field excitation is described by a generally three-dimensional (3-D) source distribution $\rho_i(\mathbf{r}'; k)$ and $\rho_j(\mathbf{r}''; k)$, which $\mathbf{r}'$ and $\mathbf{r}''$ being the position in the space of the transmit and receive antennas, respectively, and $\mathbf{s}_i$ and $\mathbf{s}_j$ denote the phase center of the antenna radiation patterns. Using convolution with the three-dimensional Green's function of the Helmholtz equation, the field excited by the source distribution is given by

$$E_i(\mathbf{r}; k) = \int_V \rho_i(\mathbf{r}'; k) \frac{\exp\left(ik|\mathbf{r} - \mathbf{s}_i - \mathbf{r}'|\right)}{4\pi|\mathbf{r} - \mathbf{s}_i - \mathbf{r}'|} d^3r' \quad (1)$$

The volume V corresponds to be volume that contains the target. It is assumed that for all antenna positions $\mathbf{r}'$ and all target positions $\mathbf{r}$, that $|\mathbf{r} - \mathbf{s}_i - \mathbf{r}'| > d^2k/\pi$, so that the far-field approximation may be applied to evaluating Eq. 1. The far-field approximation is $|\mathbf{r} - \mathbf{s}_i - \mathbf{r}'| \approx |\mathbf{r} - \mathbf{s}_i| - \frac{\mathbf{r}' \cdot (\mathbf{r} - \mathbf{s}_i)}{|\mathbf{r} - \mathbf{s}_i|}$, which applied to Eq. 1 yields:

$$E_i(\mathbf{r}; k) = \frac{\exp\left(ik|\mathbf{r} - \mathbf{s}_i|\right)}{4\pi|\mathbf{r} - \mathbf{s}_i|}$$
$$\times \int_V \rho_i(\mathbf{r}'; k) \exp\left[-ik\frac{\mathbf{r}' \cdot (\mathbf{r} - \mathbf{s}_i)}{|\mathbf{r} - \mathbf{s}_i|}\right] d^3r' \quad (2)$$

In the single scattering approximation, the detected power received at antenna j scattered from the object after being illuminated by antenna i is given by

$$P_{ij}(k) = \frac{i2\pi^2}{\eta_0 k} \int_V \chi(\mathbf{r}) E_i(\mathbf{r}; k) E_j(\mathbf{r}; k) d^3r \quad (3)$$

where η_0 is the impedance of free space, and $\chi(\mathbf{r})$ is the susceptibility of the target to be imaged. A derivation of this equation may be found as Eq. 18 in Ref. [4] in the scalar approximation. Inserting the far-field approximation of Eq. 2 for the transmit and receive fields as a function of transmit field position $\mathbf{r}'$ and receive field position $\mathbf{r}''$:

$$P_{ij}(k) = \frac{i2\pi^2}{\eta_0 k} \int_V \chi(\mathbf{r})$$
$$\times \frac{\exp\left(ik|\mathbf{r} - \mathbf{s}_i|\right)}{4\pi|\mathbf{r} - \mathbf{s}_i|} \int_V \rho_i(\mathbf{r}'; k)$$
$$\times \exp\left[-ik\frac{\mathbf{r}' \cdot (\mathbf{r} - \mathbf{s}_i)}{|\mathbf{r} - \mathbf{s}_i|}\right] d^3r'$$
$$\times \frac{\exp\left(ik|\mathbf{r} - \mathbf{s}_j|\right)}{4\pi|\mathbf{r} - \mathbf{s}_j|} \int_V \rho_j(\mathbf{r}''; k) \exp$$
$$\times \left[-ik\frac{\mathbf{r}'' \cdot (\mathbf{r} - \mathbf{s}_j)}{|\mathbf{r} - \mathbf{s}_j|}\right] d^3r'' d^3r \quad (4)$$

To express Eq. 4 in the spatial Fourier domain, the 3-D Fourier transform of the source distribution of the antennas is found as a function of spatial frequency $\mathbf{q}$:

$$\tilde{\rho}_i(\mathbf{q}; k) = \int_V \rho_i(\mathbf{r}'; k) \exp(i\mathbf{r}' \cdot \mathbf{q}) d^3r' \quad (5)$$

Inserting the Fourier transforms of the source distributions to simplify the far-field radiation patterns:

$$P_{ij}(k) = \frac{i}{8\eta_0 k} \int_V \chi(\mathbf{r})$$
$$\times \frac{\exp\left(ik|\mathbf{r} - \mathbf{s}_i|\right)}{|\mathbf{r} - \mathbf{s}_i|} \tilde{\rho}_i\left(\frac{-k(\mathbf{r} - \mathbf{s}_i)}{|\mathbf{r} - \mathbf{s}_i|}; k\right)$$
$$\times \frac{\exp\left(ik|\mathbf{r} - \mathbf{s}_j|\right)}{|\mathbf{r} - \mathbf{s}_j|} \tilde{\rho}_j\left(\frac{-k(\mathbf{r} - \mathbf{s}_j)}{|\mathbf{r} - \mathbf{s}_j|}; k\right) d^3r \quad (6)$$

The phases due to propagation from the phase centers from both antennas to a point in the volume may be combined together:

$$P_{ij}(k) = \frac{i}{8\eta_0 k} \int_V \chi(\mathbf{r})$$
$$\times \frac{\exp\left[ik\left(|\mathbf{r} - \mathbf{s}_i| + |\mathbf{r} - \mathbf{s}_j|\right)\right]}{|\mathbf{r} - \mathbf{s}_i||\mathbf{r} - \mathbf{s}_j|}$$
$$\times \tilde{\rho}_i\left(\frac{-k(\mathbf{r} - \mathbf{s}_i)}{|\mathbf{r} - \mathbf{s}_i|}; k\right) \tilde{\rho}_j\left(\frac{-k(\mathbf{r} - \mathbf{s}_j)}{|\mathbf{r} - \mathbf{s}_j|}; k\right) d^3r \quad (7)$$

To simplify further, the Fourier transform of the object $\mathbf{q}$ is found as a function of the spatial frequency $\mathbf{q}$. The position $\mathbf{r}_0$ is the nominal center of the object, and $\mathbf{q}_0$ is the nominal center spatial frequency of the object. In practice, if the volume containing the object is known, $\mathbf{r}_0$ is placed close to the center of the volume, for example, at its centroid. Similarly, $\mathbf{q}_0$ is chosen by examining the Fourier support volume of the target susceptibility that is accessible by a particular antenna and object configuration [4], and choosing $\mathbf{q}_0$ to be at the centroid of the support volume. The parameters $\mathbf{r}_0$ and $\mathbf{q}_0$ are chosen to minimize the sampling and computational burden, but do not influence the results.

$$\chi(\mathbf{r}) = \frac{1}{(2\pi)^3} \int \tilde{\chi}(\mathbf{q}) \exp\left[-i(\mathbf{r} - \mathbf{r}_0) \cdot (\mathbf{q} + \mathbf{q}_0)\right] d^3q \quad (8)$$

Inserting this Fourier transform into Eq. 7,

$$P_{ij}(k) = \frac{i}{8\eta_0 k} \int_V \frac{1}{(2\pi)^3}$$
$$\times \int \tilde{\chi}(\mathbf{q}) \exp\left[-i(\mathbf{r} - \mathbf{r}_0) \cdot (\mathbf{q} + \mathbf{q}_0)\right] d^3q$$
$$\times \frac{\exp\left[ik\left(|\mathbf{r} - \mathbf{s}_i| + |\mathbf{r} - \mathbf{s}_j|\right)\right]}{|\mathbf{r} - \mathbf{s}_i||\mathbf{r} - \mathbf{s}_j|}$$
$$\times \tilde{\rho}_i\left(\frac{-k(\mathbf{r} - \mathbf{s}_i)}{|\mathbf{r} - \mathbf{s}_i|}; k\right) \tilde{\rho}_j\left(\frac{-k(\mathbf{r} - \mathbf{s}_j)}{|\mathbf{r} - \mathbf{s}_j|}; k\right) d^3r \quad (9)$$

To further simplify this, the integration order between the **r** and **q** variables is reversed:

$$P_{ij}(k) = \frac{i}{64\pi^3\eta_0 k} \int \tilde{\chi}(\mathbf{q}) \exp[i\mathbf{r}_0 \cdot (\mathbf{q} + \mathbf{q}_0)] \int_V$$
$$\times \exp[-i\mathbf{r} \cdot (\mathbf{q} + \mathbf{q}_0)] \frac{\exp[ik(|\mathbf{r} - \mathbf{s}_i| + |\mathbf{r} - \mathbf{s}_j|)]}{|\mathbf{r} - \mathbf{s}_i||\mathbf{r} - \mathbf{s}_j|}$$
$$\times \tilde{\rho}_i\left(\frac{-k(\mathbf{r} - \mathbf{s}_i)}{|\mathbf{r} - \mathbf{s}_i|}; k\right) \tilde{\rho}_j\left(\frac{-k(\mathbf{r} - \mathbf{s}_j)}{|\mathbf{r} - \mathbf{s}_j|}; k\right) d^3r d^3q \tag{10}$$

For convenience, the vector $\mathbf{t} = \mathbf{r} - (\mathbf{s}_i + \mathbf{s}_j)/2$ is defined representing the center position between the transmit antenna i and receive antenna j, as well as their difference in position $\Delta\mathbf{s}_{ij} = (\mathbf{s}_j - \mathbf{s}_i)/2$:

$$P_{ij}(k) = \frac{i}{64\pi^3\eta_0 k} \int \tilde{\chi}(\mathbf{q}) \exp[i\mathbf{r}_0 \cdot (\mathbf{q} + \mathbf{q}_0)] \int_V$$
$$\times \exp\left[-i\left(\mathbf{t} + \frac{\mathbf{s}_i + \mathbf{s}_j}{2}\right) \cdot (\mathbf{q} + \mathbf{q}_0)\right]$$
$$\times \frac{\exp[ik(|\mathbf{t} - \Delta\mathbf{s}_{ij}| + |\mathbf{t} + \Delta\mathbf{s}_{ij}|)]}{|\mathbf{t} - \Delta\mathbf{s}_{ij}||\mathbf{t} + \Delta\mathbf{s}_{ij}|}$$
$$\times \tilde{\rho}_i\left(\frac{-k(\mathbf{t} - \Delta\mathbf{s}_{ij})}{|\mathbf{t} - \Delta\mathbf{s}_{ij}|}; k\right) \tilde{\rho}_j\left(\frac{-k(\mathbf{t} + \Delta\mathbf{s}_{ij})}{|\mathbf{t} + \Delta\mathbf{s}_{ij}|}; k\right)$$
$$\times d^3t d^3q \tag{11}$$

Examining Eq. 11, there is a rapidly varying propagation phase term:

$$\phi(\mathbf{t}) = -\left(\mathbf{t} + \frac{\mathbf{s}_i + \mathbf{s}_j}{2}\right) \cdot (\mathbf{q} + \mathbf{q}_0)$$
$$+ k(|\mathbf{t} - \Delta\mathbf{s}_{ij}| + |\mathbf{t} + \Delta\mathbf{s}_{ij}|) \tag{12}$$

If the other parts of the integrand can be assumed to be slowly spatially varying compared to this phase term, the method of stationary phase may be used to approximate this integral. The order parameter to which the stationary phase approximation is applied to is k as $k \to \infty$, however, both the radiation patterns of the antennas and the phase term depend on k. In the far-field of an antenna, the radiation pattern of the antenna, which does not include the propagation phase, varies on a much larger spatial scale than the propagation phase, which varies on a scale given by the wavelength. In practice, this means that the length $1/k$ is much smaller than the spatial scale over which the antenna radiation patterns $\tilde{\rho}_i(\mathbf{q}; k)$ vary. Therefore, while the antenna radiation patterns do vary spatially, the variation of the propagation phase term dominates the integral, and the method of stationary phase may be applied.

To $O(1/k)$, the phase propagation term is approximated by a quadratic function in the method of stationary phase, so that the integral in Eq. 11 becomes a multidimensional Gaussian integral. The value of the parts of the integrand that do not rapidly vary are approximated by a constant value at the positions $\mathbf{t}$ where $\nabla\phi = \mathbf{0}$, which are the stationary points.

These stationary points are denoted by $\mathbf{t}_p$. The oscillations caused by the phase propagation term tend to cancel out of the variations in the slowly varying components away from $\mathbf{t}_p$. The gradient of the propagation phase term is

$$\nabla\phi = -(\mathbf{q} + \mathbf{q}_0) + k\frac{\mathbf{t} - \Delta\mathbf{s}_{ij}}{|\mathbf{t} - \Delta\mathbf{s}_{ij}|} + k\frac{\mathbf{t} + \Delta\mathbf{s}_{ij}}{|\mathbf{t} + \Delta\mathbf{s}_{ij}|} \tag{13}$$

There are in general a continuous curve of stationary points $\mathbf{t}_p$ that satisfy the equation $\nabla\phi = \mathbf{0}$. Consider one such point $\mathbf{t}_p$. To find the stationary phase approximation, the quadratic approximation to the phase is found which transforms the integrand into a Gaussian integral as detailed in Ref. [37]. The quadratic approximation to the stationary phase expanded about the stationary point is:

$$\phi(\mathbf{t}) = -\left(\mathbf{t}_p + \frac{\mathbf{s}_i + \mathbf{s}_j}{2}\right) \cdot (\mathbf{q} + \mathbf{q}_0)$$
$$+ k(|\mathbf{t}_p - \Delta\mathbf{s}_{ij}| + |\mathbf{t}_p + \Delta\mathbf{s}_{ij}|)$$
$$+ \frac{1}{2}(\mathbf{t} - \mathbf{t}_p)^T \mathbf{H}(\mathbf{t} - \mathbf{t}_p)$$

$$\text{with } \mathbf{H} = \mathbf{I}\left(\frac{k}{|\mathbf{t}_p - \Delta\mathbf{s}_{ij}|} + \frac{k}{|\mathbf{t}_p + \Delta\mathbf{s}_{ij}|}\right)$$
$$- k\frac{(\mathbf{t}_p - \Delta\mathbf{s}_{ij})(\mathbf{t}_p - \Delta\mathbf{s}_{ij})^T}{|\mathbf{t}_p - \Delta\mathbf{s}_{ij}|^3}$$
$$- k\frac{(\mathbf{t}_p + \Delta\mathbf{s}_{ij})(\mathbf{t}_p + \Delta\mathbf{s}_{ij})^T}{|\mathbf{t}_p + \Delta\mathbf{s}_{ij}|^3}$$

$$\det \mathbf{H} = k^3\left(\frac{1}{|\mathbf{t}_p - \Delta\mathbf{s}_{ij}|} + \frac{1}{|\mathbf{t}_p + \Delta\mathbf{s}_{ij}|}\right)$$
$$\times \frac{1}{|\mathbf{t}_p - \Delta\mathbf{s}_{ij}|} \frac{1}{|\mathbf{t}_p + \Delta\mathbf{s}_{ij}|}$$
$$\times \left[1 - \left(\frac{(\mathbf{t}_p - \Delta\mathbf{s}_{ij})^T(\mathbf{t}_p + \Delta\mathbf{s}_{ij})}{|\mathbf{t}_p - \Delta\mathbf{s}_{ij}||\mathbf{t}_p + \Delta\mathbf{s}_{ij}|}\right)^2\right] \tag{14}$$

Inserting this quadratic approximation to $\phi(\mathbf{t})$ into Eq. 10 and holding the remainder of the integrand constant at the stationary point, the result is

$$P_{ij}(k) = \frac{i}{64\pi^3\eta_0 k} \int \tilde{\chi}(\mathbf{q}) \exp[i\mathbf{r}_0 \cdot (\mathbf{q} + \mathbf{q}_0)] \int_V$$
$$\times \exp\left[-i\left(\mathbf{t}_p + \frac{\mathbf{s}_i + \mathbf{s}_j}{2}\right) \cdot (\mathbf{q} + \mathbf{q}_0)\right.$$
$$+ ik(|\mathbf{t}_p - \Delta\mathbf{s}_{ij}| + |\mathbf{t}_p + \Delta\mathbf{s}_{ij}|)$$
$$+ \left.\frac{i}{2}(\mathbf{t} - \mathbf{t}_p)^T \mathbf{H}(\mathbf{t} - \mathbf{t}_p)\right]$$
$$\times (|\mathbf{t}_p - \Delta\mathbf{s}_{ij}||\mathbf{t}_p + \Delta\mathbf{s}_{ij}|)^{-1} \tilde{\rho}_i\left(\frac{-k(\mathbf{t}_p - \Delta\mathbf{s}_{ij})}{|\mathbf{t}_p - \Delta\mathbf{s}_{ij}|}; k\right)$$
$$\times \tilde{\rho}_j\left(\frac{-k(\mathbf{t}_p + \Delta\mathbf{s}_{ij})}{|\mathbf{t}_p + \Delta\mathbf{s}_{ij}|}; k\right) d^3t d^3q \tag{15}$$

The 3-D multidimensional Gaussian integral over $\mathbf{t}$ is now evaluated as

$$
\begin{aligned}
P_{ij}(k) = &\frac{-1}{8\pi^{3/2}\eta_0 k} \int \tilde{\chi}(\mathbf{q}) \, |\det \mathbf{H}|^{-1/2} \\
&\times \exp\left[i\left(\mathbf{r}_0 - \mathbf{t}_p - \frac{\mathbf{s}_i + \mathbf{s}_j}{2}\right)\cdot(\mathbf{q}+\mathbf{q}_0) \right.\\
&\left. + ik\left(|\mathbf{t}_p - \Delta\mathbf{s}_{ij}| + |\mathbf{t}_p + \Delta\mathbf{s}_{ij}|\right)\right]\\
&\times \left(|\mathbf{t}_p - \Delta\mathbf{s}_{ij}|\,|\mathbf{t}_p + \Delta\mathbf{s}_{ij}|\right)^{-1}\\
&\times \tilde{\rho}_i\left(\frac{-k(\mathbf{t}_p - \Delta\mathbf{s}_{ij})}{|\mathbf{t}_p - \Delta\mathbf{s}_{ij}|}; k\right)\tilde{\rho}_j\left(\frac{-k(\mathbf{t}_p + \Delta\mathbf{s}_{ij})}{|\mathbf{t}_p + \Delta\mathbf{s}_{ij}|}; k\right) d^3 q
\end{aligned}
\tag{16}
$$

Unfortunately, to perform the integration of $\mathbf{q}$, the stationary point $\mathbf{t}_p$ must be found by solving $\nabla\phi = \mathbf{0}$. As mentioned previously, there is in fact a continuous curve of solutions $\mathbf{t}_p$, and in general solving for $\mathbf{t}_p$ as a function of $\mathbf{q}$ is difficult. It is here where physical insight can help solve the problem. The stationary points correspond to the positions in the target where particular plane-wave components of the transmit and receive fields interact. If there are points of the target that are already known, rather than finding the stationary point $\mathbf{t}_p$ based on the Fourier component $\mathbf{q}$, we can parameterize the Fourier component $\mathbf{q}$ as a function of the known position $\mathbf{t}_p$. This way, only the portions of the calculation that are needed to determine the susceptibility in the target volume are performed, rather than over all Fourier components $\mathbf{q}$, as most combinations of these components do not contribute to the scattering in the target volume. The integral of Eq. 16 is reparameterized as a function of $\mathbf{t}_p$:

$$
\begin{aligned}
P_{ij}(k) = &\frac{-1}{8\pi^{3/2}\eta_0 k} \int_V \tilde{\chi}(\mathbf{q}) \\
&\times \exp\left[i\left(\mathbf{r}_0 - \mathbf{t}_p - \frac{\mathbf{s}_i + \mathbf{s}_j}{2}\right)\cdot(\mathbf{q}+\mathbf{q}_0) \right.\\
&\left. + ik\left(|\mathbf{t}_p - \Delta\mathbf{s}_{ij}| + |\mathbf{t}_p + \Delta\mathbf{s}_{ij}|\right)\right]\\
&\times |\det\mathbf{H}|^{-1/2}\left(|\mathbf{t}_p - \Delta\mathbf{s}_{ij}|\,|\mathbf{t}_p + \Delta\mathbf{s}_{ij}|\right)^{-1}\\
&\times \tilde{\rho}_i\left(\frac{-k(\mathbf{t}_p - \Delta\mathbf{s}_{ij})}{|\mathbf{t}_p - \Delta\mathbf{s}_{ij}|}; k\right)\\
&\times \tilde{\rho}_j\left(\frac{-k(\mathbf{t}_p + \Delta\mathbf{s}_{ij})}{|\mathbf{t}_p + \Delta\mathbf{s}_{ij}|}; k\right)\left|\frac{\partial^3 \mathbf{q}}{\partial \mathbf{t}_p^3}\right| d^3 t_p
\end{aligned}
\tag{17}
$$

with $\mathbf{q}$ calculated from $\mathbf{t}_p$ as given by Eq. 13:

$$
\mathbf{q} = k\frac{\mathbf{t}_p - \Delta\mathbf{s}_{ij}}{|\mathbf{t}_p - \Delta\mathbf{s}_{ij}|} + k\frac{\mathbf{t}_p + \Delta\mathbf{s}_{ij}}{|\mathbf{t}_p + \Delta\mathbf{s}_{ij}|} - \mathbf{q}_0
\tag{18}
$$

However, the calculational effort of Eq. 17 has not been significantly reduced from the model of Eq. 3. To further reduce the effort, consider two stationary points $\mathbf{t}_p$ are near each other and the corresponding two plane-wave components of the transmit and receive antennas that interact at each point given by $\mathbf{q}_i = \frac{-k(\mathbf{t}_p - \Delta\mathbf{s}_{ij})}{|\mathbf{t}_p - \Delta\mathbf{s}_{ij}|}$ and $\mathbf{q}_j = \frac{-k(\mathbf{t}_p + \Delta\mathbf{s}_{ij})}{|\mathbf{t}_p + \Delta\mathbf{s}_{ij}|}$

respectively. If the two stationary points are separated in the range direction, as radiation patterns in the far-field tend to vary slowly with range, the same two plane-wave components interact. If the two stationary points are separated in the cross range direction, the radiation patterns of the antennas may vary significantly. Therefore rather than integrating over the entire volume V, one may choose a surface S that is primarily aligned to the cross-range directions. This reduces the dimensionality of the integral from three-dimensional to two-dimensional (2-D), significantly reducing the computational effort. Rewritten as a 2-D integral:

$$
\begin{aligned}
P_{ij}(k) = &\frac{-1}{8\pi^{3/2}\eta_0 k} \int_S \tilde{\chi}(\mathbf{q}) \\
&\times \exp\left[i\left(\mathbf{r}_0 - \mathbf{t}_p - \frac{\mathbf{s}_i + \mathbf{s}_j}{2}\right)\cdot(\mathbf{q}+\mathbf{q}_0) \right.\\
&\left. + ik\left(|\mathbf{t}_p - \Delta\mathbf{s}_{ij}| + |\mathbf{t}_p + \Delta\mathbf{s}_{ij}|\right)\right]\\
&\times |\det\mathbf{H}|^{-1/2}\left(|\mathbf{t}_p - \Delta\mathbf{s}_{ij}|\,|\mathbf{t}_p + \Delta\mathbf{s}_{ij}|\right)^{-1}\\
&\times \tilde{\rho}_i\left(\frac{-k(\mathbf{t}_p - \Delta\mathbf{s}_{ij})}{|\mathbf{t}_p - \Delta\mathbf{s}_{ij}|}; k\right)\\
&\times \tilde{\rho}_j\left(\frac{-k(\mathbf{t}_p + \Delta\mathbf{s}_{ij})}{|\mathbf{t}_p + \Delta\mathbf{s}_{ij}|}; k\right)\left|\frac{\partial^2 \mathbf{q}}{\partial \mathbf{t}_p^2}\right| d^2 t_p
\end{aligned}
\tag{19}
$$

In general, the Jacobian determinant $\left|\frac{\partial^2 \mathbf{q}}{\partial \mathbf{t}_p^2}\right|$ depends on the exact shape of the surface S. However, as it is not a phase factor, approximation of this determinant do not greatly affect the target reconstruction. To look for a suitable approximation, examine the case of monostatic imaging, so that $\Delta\mathbf{s}_{ij} = \mathbf{0}$ and $\mathbf{q} = -2k\mathbf{t}_p/|\mathbf{t}_p|$. In this case $\left|\frac{\partial^2 \mathbf{q}}{\partial \mathbf{t}_p^2}\right| \approx 4k^2 |\mathbf{t}_p|^{-2}$. To account for the distance from the transmitter and receiver antennas, but approximating the angle between $\mathbf{t}_p - \Delta\mathbf{s}_{ij}$ and $\mathbf{t}_p + \Delta\mathbf{s}_{ij}$ as small, the determinant may be approximated as $\left|\frac{\partial^2 \mathbf{q}}{\partial \mathbf{t}_p^2}\right| \approx 4k^2 |(\mathbf{t}_p - \Delta\mathbf{s}_{ij})(\mathbf{t}_p + \Delta\mathbf{s}_{ij})|^{-1}$. This approximation, however, is expected to fail when the transmitter and receiver are on opposite sides of the target. Inserting this approximation to the Jacobian determinant:

$$
\begin{aligned}
P_{ij}(k) = &\frac{-k}{2\pi^{3/2}\eta_0} \int_S \tilde{\chi}(\mathbf{q}) \\
&\times \exp\left[i\left(\mathbf{r}_0 - \mathbf{t}_p - \frac{\mathbf{s}_i + \mathbf{s}_j}{2}\right)\cdot(\mathbf{q}+\mathbf{q}_0) \right.\\
&\left. + ik\left(|\mathbf{t}_p - \Delta\mathbf{s}_{ij}| + |\mathbf{t}_p + \Delta\mathbf{s}_{ij}|\right)\right]\\
&\times |\det\mathbf{H}|^{-1/2}\left(|\mathbf{t}_p - \Delta\mathbf{s}_{ij}|\,|\mathbf{t}_p + \Delta\mathbf{s}_{ij}|\right)^{-2}\\
&\times \tilde{\rho}_i\left(\frac{-k(\mathbf{t}_p - \Delta\mathbf{s}_{ij})}{|\mathbf{t}_p - \Delta\mathbf{s}_{ij}|}; k\right)\tilde{\rho}_j\left(\frac{-k(\mathbf{t}_p + \Delta\mathbf{s}_{ij})}{|\mathbf{t}_p + \Delta\mathbf{s}_{ij}|}; k\right) d^2 t_p
\end{aligned}
\tag{20}
$$
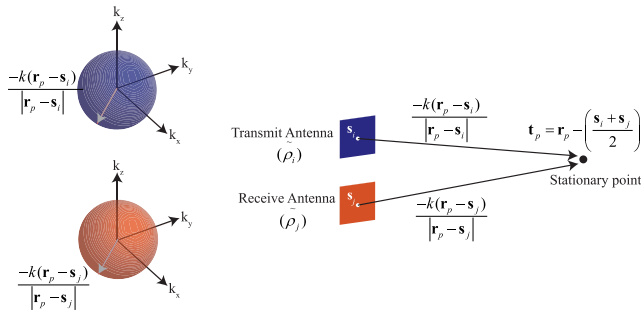
FIGURE 2. A diagram showing the plane-wave components of the transmit and receive antennas that contribute to the reconstruction in the vicinity of a stationary point $\mathbf{r}_p$. Only the plane-wave with the spatial frequency $-\frac{k(\mathbf{r}_p - \mathbf{s}_i)}{|\mathbf{r}_p - \mathbf{s}_i|}$ radiated from the transmit antenna is incident on the point $\mathbf{r}_p$, and only the spatial frequency $-\frac{k(\mathbf{r}_p - \mathbf{s}_j)}{|\mathbf{r}_p - \mathbf{s}_j|}$ can be received from the field scattered by volume of the target centered at the point $\mathbf{t}_p$. Therefore only the spatial frequency $\mathbf{q} = -\frac{k(\mathbf{r}_p - \mathbf{s}_i)}{|\mathbf{r}_p - \mathbf{s}_i|} - \frac{k(\mathbf{r}_p - \mathbf{s}_j)}{|\mathbf{r}_p - \mathbf{s}_j|}$ can be probed of the target for this particular stationary point.

Eq. 20 is now in a form that may be efficiently calculated. The surface of stationary points $\mathbf{t}_p$ may be selected to minimize the computational effort as they may be placed in the vicinity of the target. Furthermore, only a two-dimensional surface of points in the three-dimensional target volume are required. Unlike Eq. 3, which integrates a highly oscillatory Green's function and therefore must be sampled at subwavelength intervals to produce an accurate result, Eq. 20 operates in the Fourier space of the target, and therefore the reconstruction may be limited to reduce the computational burden without aliasing. The parameters $\mathbf{r}_0$ and $\mathbf{q}_0$ allow the Fourier transform of the object $\tilde{\chi}(\mathbf{q})$ to be stored and processed with the minimum number of samples by offsetting the target in real space and frequency space to a known center position and center spatial frequency at which the target is reconstructed. Finally, operations in the Fourier space of the antenna and target map well onto the geometric operations intrinsic to real-time graphics rendering.

To understand the meaning of the stationary phase approximation in this case, we consider two antennas and a particular stationary point $\mathbf{r}_p = \mathbf{t}_p + \frac{\mathbf{s}_i + \mathbf{s}_j}{2}$, as shown in Fig. 2. As the entire target, including the stationary points in the target volume, are in the far-field of the antennas, only one plane-wave component is incident on the stationary point from each antenna. All of these plane-wave components are on a sphere of k radius from the origin of the Fourier space of the fields. For the transmit antenna, the plane-wave component with the spatial frequency $-\frac{k(\mathbf{r}_p - \mathbf{s}_i)}{|\mathbf{r}_p - \mathbf{s}_i|}$ is incident on the target, while the receive antenna only captures the plane-wave component $-\frac{k(\mathbf{r}_p - \mathbf{s}_j)}{|\mathbf{r}_p - \mathbf{s}_j|}$ scattered from the target around the region of the stationary point. Therefore only the spatial frequency $\mathbf{q} = -\frac{k(\mathbf{r}_p - \mathbf{s}_i)}{|\mathbf{r}_p - \mathbf{s}_i|} - \frac{k(\mathbf{r}_p - \mathbf{s}_j)}{|\mathbf{r}_p - \mathbf{s}_j|}$ of the object can be probed using this stationary point for this transmit and receive antenna pair.

III. IMPLEMENTATION OF FAMI

Eq. 20 is an approximation to Eq. 3 with the stated approximations, however, additional implementation details must be specified to numerically perform the computation. The implementation used in the simulation is described here and provides good accuracy and performance and is suitable for GPGPU computation. Both the forward operator of Eq. 20 to calculate the measurements $P_{ij}(k)$ from the target susceptibility $\tilde{\chi}(\mathbf{q})$ and the adjoint is provided which is used to calculate an estimate of $\tilde{\chi}(\mathbf{q})$ from $P_{ij}(k)$.

For the implementation it is assumed that the antennas are two-dimensional, planar antennas with their surfaces normal to the range direction. As the field produced by a three-dimensional antenna can be produced by an equivalent source on a surface, a planar source may always be found that reproduces the three-dimensional antenna field. By transforming the antenna fields to a common coordinate system and storing these transformed fields, the computational effort of transformation need only be performed once for a particular antenna configuration. Rotating the fields to a common coordinate system may be performed by representing the fields as plane waves, and interpolating the uniformly spaced spatial frequencies sampled in the new coordinate system as a function of the old coordinates using a rotation matrix to relate the spatial frequencies of the new and old spatial frequency vectors. It is easiest to leave the phase center of the antenna unchanged and rotate the fields around the phase center. If vector-valued polarized fields are used, the polarization must be rotated at the same time using the same rotation matrix. As it is the plane-wave representation of the radiation pattern that must be stored to apply Eq. 20, the transformed plane-wave representation of the antenna patterns needed for FAMI are directly obtained.

To avoid confusion because of the large number of variables used, Table 1 lists the specified quantities that represent the antennas and target based on the physical parameters of the MIMO radar system, and Table 2 is a table of the quantities that are derived from the quantities of Table 1. The x and y dimensions are the cross-range directions, and the z dimension is the range direction. As Eq. 20 operates on the Fourier transforms of the antenna radiation patterns $\tilde{\rho}_i(\mathbf{q}; k)$ and target susceptibility $\tilde{\chi}(\mathbf{q})$, these are represented by a uniformly sampled, spatially bandlimited function. The antenna radiation patterns are sampled in the cross-range range direction at intervals of ΔX and ΔY as the array $\rho_{nm,ij}$, where n and m are the sampled indices $-N_x/2 \leq n \leq N_x/2 - 1$ and $-N_y/2 \leq m \leq N_y/2 - 1$, i is the index of the illumination spatial frequency k_i, and j is the index of the antenna. The discrete Fourier transform with respect to n and m is the quantity $\tilde{\rho}_{nm,i}$, with the spatial frequencies in the cross-range direction sampled at intervals of $\Delta Q_x = 1/(N_x \Delta X)$ and $\Delta Q_y = 1/(N_y \Delta Y)$. Therefore a particular sample of the antenna's discrete Fourier transform represents a spatial frequency $\mathbf{q}_{nm,ij} = \Delta Q_x n \hat{\mathbf{x}} + \Delta Q_y m \hat{\mathbf{y}} + \sqrt{(k_i/2\pi)^2 - (\Delta Q_x n)^2 - (\Delta Q_y m)^2} \hat{\mathbf{z}}$ so

TABLE 1. Definitions of quantities.

Symbol	Units	Description
χ_{ijk}	unitless	Target susceptibility samples, indexed by cross-range i, j and range k position
n_x, n_y	count	Number of samples in cross-range directions
n_z	count	Number of samples in range direction
$\Delta x, \Delta y$	distance	Sample spacing of susceptibility in cross-range directions
Δz	distance	Sample spacing of susceptibility in range direction
P_{ijk}	power	Measured power scattered from object from antennas i and j at frequency indexed by k
$\rho_{nm,ij}$	unitless	Source density at frequency i of antenna j as a function of spatial indices n, m
N_x, N_y	count	Number of samples of the source antenna density
$\Delta X, \Delta Y$	distance	Sample spacing in cross-range direction of the antenna source density
$\mathbf{s}_j$	distance vector	Phase center position of antenna j
k_i	spatial frequency	List of spatial frequencies for which data is collected indexed by i.
$\mathbf{t}_p$	distance vector	Positions of stationary points
$\mathbf{r}_0$	distance vector	Center of target susceptibility volume
$\mathbf{q}_0$	spatial frequency vector	Center spatial frequency of target susceptibility

TABLE 2. Derived quantities.

Symbol	Units	Description
$\tilde{\chi}_{ijk}$	unitless	Three-dimensional discrete Fourier transform of χ_{ijk}
Δq_x	spatial frequency	Spatial frequency sampling rate of target, cross-range $\Delta q_x = 1/(n_x \Delta x)$
Δq_y	spatial frequency	Spatial frequency sampling rate of target, cross-range $\Delta q_y = 1/(n_y \Delta y)$
Δq_z	spatial frequency	Spatial frequency sampling rate of target $\Delta q_z = 1/(n_z \Delta z)$
$\tilde{\rho}_{nm,ij}$	unitless	Two-dimensional discrete Fourier transform of $\rho_{nm,ij}$ with respect to indices n, m
ΔQ_x	spatial frequency	Spatial frequency sampling rate of antenna field $\Delta Q_x = 1/(N_x \Delta X)$
ΔQ_y	spatial frequency	Spatial frequency sampling rate of antenna field $\Delta Q_y = 1/(N_y \Delta Y)$
$\Delta \mathbf{s}_{ij}$	distance vector	Distance between phase centers i and j $\Delta \mathbf{s}_{ij} = (\mathbf{s}_j - \mathbf{s}_i)/2$

that the spatial frequency is on the k-sphere corresponding to radiated waves.

Likewise, the target susceptibility is stored as a $n_x \times n_y \times n_z$ three-dimensional array χ_{ijk}, which is sampled at regular intervals Δx and Δy in the cross-range direction, and Δz in the range direction, with the indices $-n_x/2 \le i \le n_x/2-1$, $-n_y/2 \le j \le n_y/2 - 1$, and $-n_z/2 \le k \le n_z/2 - 1$. The 3-D discrete Fourier transform of this target susceptibility is stored as $\tilde{\chi}_{ijk}$, with the spacing of spatial frequencies in the cross-range direction being $\Delta q_x = 1/(n_x \Delta x)$ and $\Delta q_y = 1/(n_y \Delta y)$, and in the range direction being $\Delta q_z = 1/(n_z \Delta z)$. Therefore a sample of the spatial frequency of the object represents the spatial frequency $\mathbf{q}_{ijk} = \Delta q_x i\hat{\mathbf{x}} + \Delta q_y j\hat{\mathbf{x}} + \Delta q_z k\hat{\mathbf{z}}$. Finally, the list of stationary points that correspond to the target surface are given by $\mathbf{t}_p$.

With the relevant quantities defined, a description of the forward operator is now given (as shown in the pseudocode labeled Algorithm 1 below). As a precalculation step for both the forward and adjoint operators, the discrete Fourier transform of the source density of the antennas $\rho_{nm,ij}$ may be stored as $\tilde{\rho}_{nm,ij}$. The first step of the method is to calculate the 3-D discrete Fourier transform (usually using the Fast Fourier Transform) of the sampled susceptibility χ_{ijk} as $\tilde{\chi}_{ijk}$. To calculate the measurements P_{ijd} from $\tilde{\chi}_{ijk}$, the following

sum is performed:

$$
\begin{aligned}
P_{ijd} = \sum_{\mathbf{t}_p, k_d} & \frac{-k_d}{2\pi^{3/2}\eta_0} \tilde{\chi}(\mathbf{q}) \\
& \times \tilde{\rho}_i \left(\frac{-k_d(\mathbf{t}_p - \Delta\mathbf{s}_{ij})}{|\mathbf{t}_p - \Delta\mathbf{s}_{ij}|}; k \right) \tilde{\rho}_j \left(\frac{-k_d(\mathbf{t}_p + \Delta\mathbf{s}_{ij})}{|\mathbf{t}_p + \Delta\mathbf{s}_{ij}|}; k \right) \\
& \times \exp\left[i \left(\mathbf{r}_0 - \mathbf{t}_p - \frac{\mathbf{s}_i + \mathbf{s}_j}{2} \right) \cdot (\mathbf{q} + \mathbf{q}_0) \right. \\
& \left. + ik_d \left(|\mathbf{t}_p - \Delta\mathbf{s}_{ij}| + |\mathbf{t}_p + \Delta\mathbf{s}_{ij}| \right) \right] \\
& \times |\det \mathbf{H}|^{-1/2} \left(|\mathbf{t}_p - \Delta\mathbf{s}_{ij}| \, |\mathbf{t}_p + \Delta\mathbf{s}_{ij}| \right)^{-2}
\end{aligned}
$$

$$
\text{with } \mathbf{q} = k_d \frac{\mathbf{t}_p - \Delta\mathbf{s}_{ij}}{|\mathbf{t}_p - \Delta\mathbf{s}_{ij}|} + k_d \frac{\mathbf{t}_p + \Delta\mathbf{s}_{ij}}{|\mathbf{t}_p + \Delta\mathbf{s}_{ij}|} - \mathbf{q}_0 \tag{21}
$$

The sum of Eq. 21 is performed over all stationary points and frequencies. One complicating factor is that the spatial frequencies $\mathbf{q}$ on which the susceptibility $\tilde{\chi}(\mathbf{q})$ is sampled do not generally correspond to known samples, rather these are in between known samples. Therefore a method of interpolation is needed to estimate the desired samples from the known samples, for example, nearest neighbor or trilinear interpolation. The indices of the spatial frequencies of the sampled Fourier transform $\tilde{\chi}_{ijk}$ are given by $i = (\mathbf{q} \cdot \hat{\mathbf{x}})/\Delta q_x$, $j = (\mathbf{q} \cdot \hat{\mathbf{y}})/\Delta q_y$, and $k = (\mathbf{q} \cdot \hat{\mathbf{z}})/\Delta q_z$. As $\mathbf{q}$ depends on the position of the stationary point $\mathbf{t}_p$ as well as the phase centers $\mathbf{s}_i$ and $\mathbf{s}_j$, the samples of $\tilde{\chi}(\mathbf{q})$ required are determined by the geometry of the antenna and target positions. Physically, this is because the available Fourier space that may be sampled of the target is determined by this geometry, and therefore one may not arbitrarily choose the Fourier space support of the object. Interpolation must also be performed to calculate $\tilde{\rho}_i(\cdot)$ as these are also sampled on a uniform grid, and the

frequencies $\frac{-k_d(\mathbf{t}_p - \Delta\mathbf{s}_{ij})}{|\mathbf{t}_p - \Delta\mathbf{s}_{ij}|}$ and $\frac{-k_d(\mathbf{t}_p + \Delta\mathbf{s}_{ij})}{|\mathbf{t}_p + \Delta\mathbf{s}_{ij}|}$ do not necessarily correspond to these samples, for example using a nearest neighbor or bilinear interpolator.

Algorithm 1 Forward operator

1: $P_{ijd} \leftarrow 0$.
2: Take the 3-D discrete Fourier transform of χ_{abc} to yield $\tilde{\chi}_{abc}$.
3: **for** all antenna pairs i, j, stationary points $\mathbf{t}_p$ and frequencies k_d **do**
4:     Calculate $\mathbf{q} = k_d \frac{\mathbf{t}_p - \Delta\mathbf{s}_{ij}}{|\mathbf{t}_p - \Delta\mathbf{s}_{ij}|} + k_d \frac{\mathbf{t}_p + \Delta\mathbf{s}_{ij}}{|\mathbf{t}_p + \Delta\mathbf{s}_{ij}|} - \mathbf{q}_0$
5:     Calculate
$$P_{ijd} \leftarrow P_{ijd} + \tilde{\chi}(\mathbf{q}) \frac{-k_d}{2\pi^{3/2}\eta_0}$$
$$\tilde{\rho}_i \left(\frac{-k_d(\mathbf{t}_p - \Delta\mathbf{s}_{ij})}{|\mathbf{t}_p - \Delta\mathbf{s}_{ij}|}; k \right) \tilde{\rho}_j \left(\frac{-k_d(\mathbf{t}_p + \Delta\mathbf{s}_{ij})}{|\mathbf{t}_p + \Delta\mathbf{s}_{ij}|}; k \right)$$
$$\exp\left[i \left(\mathbf{r}_0 - \mathbf{t}_p - \frac{\mathbf{s}_i + \mathbf{s}_j}{2} \right) \cdot (\mathbf{q} + \mathbf{q}_0) + ik_d \left(|\mathbf{t}_p - \Delta\mathbf{s}_{ij}| + |\mathbf{t}_p + \Delta\mathbf{s}_{ij}| \right) \right]$$
$$|\det \mathbf{H}|^{-1/2} \left(|\mathbf{t}_p - \Delta\mathbf{s}_{ij}| \, |\mathbf{t}_p + \Delta\mathbf{s}_{ij}| \right)^{-2}$$
6: **end for**

The adjoint operator is somewhat more complicated because of the interpolation step. The linear operation corresponding to the adjoint is given by

$$\tilde{\chi}(\mathbf{q}) = \sum_{i,j,\mathbf{t}_p,k_d} \frac{-k_d}{2\pi^{3/2}\eta_0} P_{ijd}$$
$$\times \tilde{\rho}_i \left(\frac{-k_d(\mathbf{t}_p - \Delta\mathbf{s}_{ij})}{|\mathbf{t}_p - \Delta\mathbf{s}_{ij}|}; k \right)^* \tilde{\rho}_j \left(\frac{-k_d(\mathbf{t}_p + \Delta\mathbf{s}_{ij})}{|\mathbf{t}_p + \Delta\mathbf{s}_{ij}|}; k \right)^*$$
$$\times \exp\left[-i \left(\mathbf{r}_0 - \mathbf{t}_p - \frac{\mathbf{s}_i + \mathbf{s}_j}{2} \right) \cdot (\mathbf{q} + \mathbf{q}_0) \right.$$
$$\left. - ik_d \left(|\mathbf{t}_p - \Delta\mathbf{s}_{ij}| + |\mathbf{t}_p + \Delta\mathbf{s}_{ij}| \right) \right]$$
$$\times |\det \mathbf{H}|^{-1/2} \left(|\mathbf{t}_p - \Delta\mathbf{s}_{ij}| \, |\mathbf{t}_p + \Delta\mathbf{s}_{ij}| \right)^{-2}$$

(22)

In practice, one would like to calculate $\tilde{\chi}(\mathbf{q})$ on a uniform grid to apply the inverse 3-D Fourier transform to recover χ_{ijk}. However, as noted during calculation of the forward operator, the samples of Fourier data depend on the stationary point and target positions and therefore are generally not sampled uniformly. While for the forward operator, samples of the Fourier data may be interpolated, for the adjoint operator the samples must be updated. As the samples are stored on a uniform grid, a method is needed to update the samples on a uniform grid given updates of spatial frequencies $\mathbf{q}$ that do not correspond to samples on the grid. This operation may be seen as the adjoint operation of the interpolation step. An interpolator takes a weighted sum of samples surrounding a spatial frequency to produce an estimate of the susceptibility at that spatial frequency. To update a spatial frequency using the adjoint of the interpolation step, one adds the weighted susceptibility at that spatial frequency to the samples that determined the susceptibility to be updated. As interpolators generally apply the largest magnitude weights to samples nearest to the interpolated point, the adjoint of the interpolator

adds the largest contribution of the interpolated points to samples near the point.

In practice, this may be achieved by updating two arrays, a cumulative array of samples $\tilde{\chi}'_{abc}$ in the Fourier space, and a corresponding cumulative array of weights w_{abc}. The cumulative array of weights accounts for the contributions of each updated point to a given sample. The function $W(\mathbf{q}, \mathbf{q}_r)$ is the magnitude of the weight of a point at $\mathbf{q}_r$ to a sample at point $\mathbf{q}$, which is usually a decreasing function of $|\mathbf{q} - \mathbf{q}_r|$. The pseudocode of the algorithm to implement the adjoint operator using the cumulative array of weights to perform the adjoint interpolation step is given in the below pseudocode labeled Algorithm 2:

Algorithm 2 Adjoint operator

1: $\tilde{\chi}'_{abc} \leftarrow 0, w_{abc} \leftarrow 0$.
2: **for** all antenna pairs i, j, stationary points $\mathbf{t}_p$ and frequencies k_d **do**
3:     Calculate $\mathbf{q} = k_d \frac{\mathbf{t}_p - \Delta\mathbf{s}_{ij}}{|\mathbf{t}_p - \Delta\mathbf{s}_{ij}|} + k_d \frac{\mathbf{t}_p + \Delta\mathbf{s}_{ij}}{|\mathbf{t}_p + \Delta\mathbf{s}_{ij}|} - \mathbf{q}_0$
4:     Calculate $a = \text{round}\left(\frac{\mathbf{q} \cdot \hat{\mathbf{x}}}{\Delta q_x} \right)$, $b = \text{round}\left(\frac{\mathbf{q} \cdot \hat{\mathbf{y}}}{\Delta q_y} \right)$, and $c = \text{round}\left(\frac{\mathbf{q} \cdot \hat{\mathbf{z}}}{\Delta q_z} \right)$ with round being the nearest integer function.
5:     Calculate $\mathbf{q}_r = a\Delta q_x \hat{\mathbf{x}} + b\Delta q_y \hat{\mathbf{y}} + c\Delta q_z \hat{\mathbf{z}}$
6:     Accumulate susceptibility
$$\tilde{\chi}'_{abc} \leftarrow \tilde{\chi}'_{abc} +$$
$$W(\mathbf{q}, \mathbf{q}_r) P_{ijd} \frac{-k_d}{2\pi^{3/2}\eta_0}$$
$$\tilde{\rho}_i \left(\frac{-k_d(\mathbf{t}_p - \Delta\mathbf{s}_{ij})}{|\mathbf{t}_p - \Delta\mathbf{s}_{ij}|}; k \right)^* \tilde{\rho}_j \left(\frac{-k_d(\mathbf{t}_p + \Delta\mathbf{s}_{ij})}{|\mathbf{t}_p + \Delta\mathbf{s}_{ij}|}; k \right)^*$$
$$\exp\left[-i \left(\mathbf{r}_0 - \mathbf{t}_p - \frac{\mathbf{s}_i + \mathbf{s}_j}{2} \right) \cdot (\mathbf{q} + \mathbf{q}_0) - ik_d \left(|\mathbf{t}_p - \Delta\mathbf{s}_{ij}| + |\mathbf{t}_p + \Delta\mathbf{s}_{ij}| \right) \right]$$
$$|\det \mathbf{H}|^{-1/2} \left(|\mathbf{t}_p - \Delta\mathbf{s}_{ij}| \, |\mathbf{t}_p + \Delta\mathbf{s}_{ij}| \right)^{-2}$$
7:     Accumulate weights $w_{abc} \leftarrow w_{abc} + W(\mathbf{q}, \mathbf{q}_r)$
8: **end for**
9: Divide weights $\tilde{\chi}_{abc} \leftarrow \tilde{\chi}'_{abc} / w_{abc}$, with the case $\frac{0}{0} = 0$.
10: Take the inverse 3-D discrete Fourier transform of $\tilde{\chi}_{abc}$ to yield χ_{abc}.

The sampling of stationary points $\mathbf{t}_p$ must be sufficiently dense to ensure that all points $\tilde{\chi}_{abc}$ are updated within the Fourier support of the object at least once.

IV. ADAPTATION OF FAMI TO A GPGPU

One of the practical benefits of the algorithms described in section III is the correspondence of operations to those accelerated by GPGPU hardware. Because many of the operations on the sampled susceptibility and antenna functions are similar to those already designed into GPGPU hardware, especially texture mapping, texel retrieval, and projection operations, the same hardware logic that is used to retrieve and cache textures may be used to retrieve and cache antenna radiation patterns and the sample susceptibility. The plane-wave components of the antenna radiation patterns may be retrieved and projected in the same way rays are rendered to the computer display by the GPU, with the main difference

being that while rays for display are represented by a vector of color channel values (e.g. red, green, blue, and alpha), the representation of the field amplitude of a plane-wave component is a floating-point complex number. As modern GPGPU hardware internally represents quantities using floating point arithmetic, the texture mapping hardware is easily adapted to representing the plane-wave representation of an electromagnetic field.

Examining this correspondence further, during the display of three-dimensional objects, GPGPU hardware projects polygons to the display by traversing a list of visible points on the surface of each polygon, retrieving the corresponding texel to each point, and then overlaying the retrieved texels with the pixels already on the display. The forward and adjoint operations have a similar structure. Instead of the traversed points being the visible points on the polygonal surfaces of the object, the stationary points $\mathbf{t}_p$ correspond to the front surface of the object to be reconstructed. The "display" to which the results are accumulated corresponds to $P_{ij}(k)$ for the forward operation, or $\tilde{\chi}(\mathbf{q})$ for the adjoint operation. The textures from which texels are retrieved correspond to the plane-wave representation of the antenna radiation patterns. The implementation of the forward and adjoint operators is similar to the pixel processing pipeline already present in the GPGPUs.

Therefore in order to advantageously use the GPGPU pixel processing pipeline components to accelerate FAMI, one should put the antenna far-field radiation pattern samples $\tilde{\rho}_{nm,ij}$ into 3-D textures as a function of plane-wave component indices n and m and frequency i, with the far-fields for each antenna j in separate textures. As the texture units are designed to cache texels based on their proximity to each other in the texture, and typical access patterns of FAMI tend to sequentially retrieve samples that are near each other in space and frequency, the caching of the antenna radiation patterns as texels results in fewer cache misses during texel retrieval. As the penalty for a cache miss is high for modern GPGPUs, it is crucial to tailor the memory access patterns to best exploit the cache. Furthermore, the input vectors, which are $\tilde{\chi}(\mathbf{q})$ for the forward operator, and $P_{ij}(k)$ for the adjoint operator, may also be stored in textures to improve the caching of these as well.

Because of the superposition principle of the forward and adjoint linear operators, the computation may be parceled to multiple GPGPU units and the result of the calculations of each GPGPU summed to yield the final result. This is analogous to how the Scalable Link Interface (SLI) is used to render graphics to the same display using multiple GPGPUs. The work of computing the operator for different antenna pairs i and j may be distributed to different GPGPUs. By having each GPGPU operate on different antenna pairs, the memory cache in the GPGPU can be dedicated to accelerating access to only the antenna radiation patterns needed for its portion of the computation. As the speed of computation is usually limited by the available memory bandwidth rather than the number of available compute units, one of the main
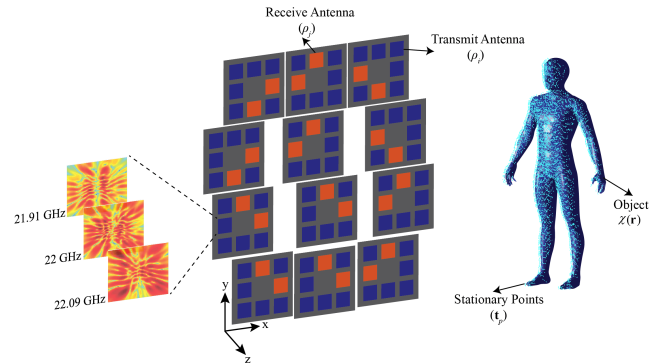

FIGURE 3. A diagram of the overall system, showing the layout of the transmit antennas (red) and receive antennas (blue). At the left, an example of the amplitude of the radiation pattern of a receive is shown at three frequencies separated by 90 MHz to demonstrate the rapid variation of radiation pattern with frequency.

benefits of using multiple GPGPU units is that each has an independent memory bus that can simultaneously access and cache its own copy of the antenna radiation patterns. Because FAMI is embarrassingly parallelizable if different antenna patterns may be distributed to different compute units, the computation speed tends to scale well with added GPGPUs, with the limitations in scaling dominated by the need to distribute and retrieve the results of computations. For real-time applications, the communication between the GPGPUs must be carefully designed as to minimize the latency as the latency may begin to dominate the reconstruction time.

V. IMAGE FORMATION USING THE GPGPU IMPLEMENTATION

To implement and demonstrate FAMI, the algorithm was programmed as NVIDIA CUDA 8.0 and C++. The implementation of FAMI closely follows the descriptions of Sections III and IV. The GPGPU hardware consisted of four NVIDIA Geforce GTX 1080 graphics processors in a SLI configuration, which were contained in an Intel Core i7-5930K CPU personal computer with 128 gigabytes of random access memory (RAM). The software is interfaced to as a MATLAB MEX file. The compilation used Visual Studio 2013 under Windows 7, and GCC 4.8.4 under Linux 3.13 as well as the nvcc CUDA 8.0 compiler. As the typical speed of the adjoint image formation process is less than 200 ms, the latency introduced by MATLAB is a significant component of the processing time, however, MATLAB was used because it is a convenient platform for prototyping numerical algorithms. It is likely that a real-time practical implementation would not use MATLAB.

The simulated system has been described previously, a diagram of which is shown in Fig. 3. Briefly summarized, the system consists of 24 transmit antennas and 72 receive antennas, operated at 100 uniformly spaced frequencies between 17 and 26 GHz. Each of the 24 transmit antennas is nearly identical and produces similar radiation patterns as frequency is varied, and the 72 receive antenna produces radiation patterns nearly identical to each other but different than that of the transmit antennas. The antennas are high Q planar
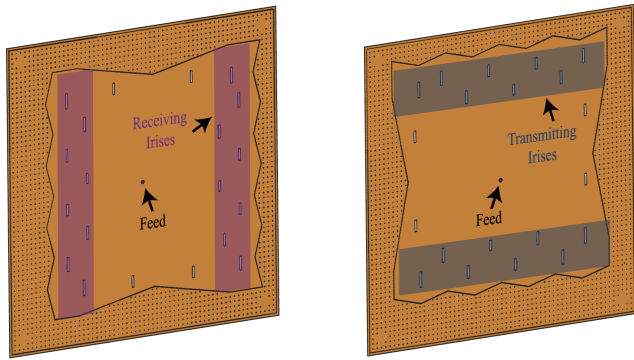
FIGURE 4. A diagram of the receiving antenna (left) and the transmitting antenna (right) showing the layout and shape of the radiating apertures, as well as the "zig-zag" line of vias that define the boundary of the cavity.

resonators that have radiating apertures on them in a Mills cross array pattern, with two 8 cm long rows of apertures oriented horizontally and separated by 8 cm vertically on the transmit antennas, and two 8 cm long columns of apertures oriented vertically and separated by 8 cm horizontally on the receive antennas. The apertures on all antennas are vertically oriented slots as to primarily transmit and receive in the vertical polarization so that a scalar approximation to the electromagnetic field may be used which corresponds to the electric response and material susceptibility in the vertical direction. Due to the irregular cavity shape of the transmit and receive antennas, the phase and amplitude of the radiation from the apertures varies in a fixed, pseudorandom pattern as the frequency is varied. The strong variation in radiation pattern with frequency enables frequency-diversity imaging techniques to be used with this system. A diagram of the antennas is shown in Fig. 4

The antennas are arranged on a planar surface 2 m by 2 m in size. The object is nominally 1.3 m from the antenna surfaces. The far-field distance from each antenna is 0.85 m, so the object is in the radiation zone of all the antennas. The depth of field of the 2 m by 2 m aperture is approximately 13 mm, so that the best image is formed within about one wavelength from the surface of the stationary phase points. The layout of the transmit and receive antennas is shown in Fig 3. This particular geometry of transmit and receive antennas is designed for security checkpoint scanning [38], [39], and therefore as a test object we chose a model of a human form to test FAMI. A mesh of uniformly scattering susceptibility points are placed on the surface of the human form to model the skin surface reflectivity. As flesh is largely reflective at the frequencies used, the reconstruction should be close to the subject's surface, and therefore the stationary points should be placed near the skin. This surface may be located approximately in practice by using a machine vision system to illuminate the subject and determine the shape of the visible surface which is meshed into a list of stationary points.

A couple of modifications were made to the algorithm to produce a reconstruction similar to the previous Virtualizer software. First, the factor of $|\det \mathbf{H}|^{-1/2}$ in Eq. 20

that accounts for the relative orientation of the stationary point to the transmit and receive antennas is changed to $|\det \mathbf{H}|^{1/2}$ in the forward and adjoint operators. When the $-\frac{1}{2}$ exponent is used, the Hessian factor is singular when the transmit and receive antennas are nearly colocated, which produced singular features on the stationary phase surface. As an inverse of the forward operator would tend to compensate for the Hessian factor, the reciprocal of the Hessian factor, the $\frac{1}{2}$ exponent, was applied instead. A second improvement takes advantage of the fact that the objects are surface objects, and therefore scattering points tend to be near other scattering points. After the adjoint operation was calculated, an "envelope function" was applied that convolves the magnitude of the susceptibility of the object with a Gaussian kernel:

$$\chi_E(\mathbf{r}) = \frac{1}{(2\pi r_0)^{3/2}} \int_V |\chi(\mathbf{r}')| \exp\left(-\frac{|\mathbf{r}'-\mathbf{r}|^2}{2r_0^2}\right) d^3 r' \quad (23)$$

where $\mathbf{r}_0$ is a window size, usually a few resolution cells in width. The susceptibility $\chi(\mathbf{r})$ is then multiplied by this envelope function $\chi_E(\mathbf{r})$, and then normalized to have the same squared magnitude signal as before multiplying by the envelope function. The effect of this nonlinear filter is to prefer points with high magnitude that are near other points, and suppress others. For surface objects, this filter greatly reduces the noise and concentrates energy onto a surface.

To serve as a benchmark for FAMI's performance, the Virtualizer, a tool for the simulation and reconstruction of coherent images that performs Eq. 3 directly, which is also optimized for GPGPU acceleration, is used. Unlike the FAMI implementation, the Virtualizer code does not take advantage of multiple GPUs for computation. To reconstruct the target, the Virtualizer performs the sum of Eq. 3 for each point to be reconstructed in a volume. The volume conforms to the surface of the target and extends in range several wavelengths away from the target towards the antenna array. The Virtualizer creates a lookup table and partitions the volume to efficiently store the three-dimensional radiation patterns of the antennas at each frequency for rapid retrieval to minimize GPGPU memory bandwidth consumption [12]. On the other hand, the sum of Eq. 20 need only be performed over the surface of stationary points on the surface of the target rather than in a volume, but the volume is reconstructed near this surface. Only the far-field radiation patterns of the antennas need to be stored, rather than three-dimensional radiation patterns. For FAMI, the stationary points on the surface of the target were placed in a rectangular grid at half a wavelength, or 7.5 mm, intervals. To reconstruct the edges of the object, the surface of the stationary points must be extended 3 to 4 wavelengths beyond the edge in order that constructive interference occurs on the surface at the boundary and destructive interference outside the boundary, so that the reconstruction on the surface is well-defined.

For comparison, we first image a simple target, consisting of an array of point-scatters seperated by a distance of 10 cm
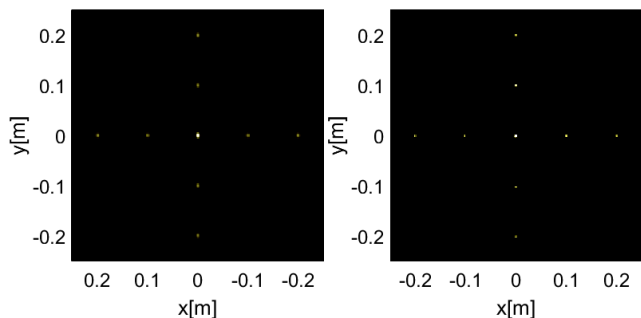
FIGURE 5. A comparison of the least-squares reconstructions of a multi-scatter point target using the Virtualizer (left) and the FAMI reconstruction (right). The dynamic range for plotting is 20 dB.
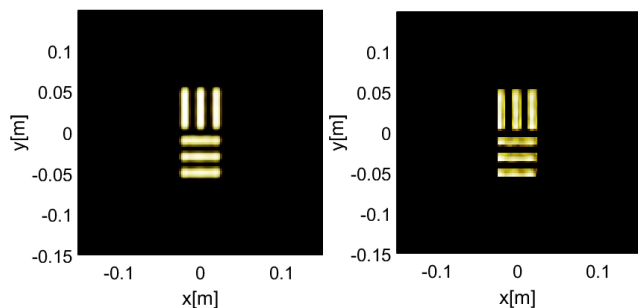
FIGURE 6. A comparison of the least-squares reconstructions of a 1 cm resolution target using the Virtualizer (left) and the FAMI reconstruction (right). The dynamic range for plotting is 20 dB.

from each other in the cross-range. Imaging of the point-scatter target is important in that it enables the analysis of the transfer fuction of the system by means of the point spread function (PSF). For image reconstruction, least-squares technique is used. The least-squares solution is 5 iterations of the conjugate gradient algorithm applied to the normal equations, with each iteration applying the forward and adjoint operators once for both the Virtualizer and FAMI, the results of which are shown in Fig. 5.

Analyzing the reconstructed images in Fig. 5, it is evident that both reconstructons are similar. The full-width-half-maximum (FWHM) values for the Virtualizer and FAMI reconstructions are obtained to be 5.02 mm and 5.06 mm, respectively. A significant advantage of the FAMI algorithm can be appreciated when the reconstruction times are compared. While the Virtualizer reconstruction takes 5.71 s, the FAMI completes the reconstruction in 0.2 s, corresponding to a speed-up by a factor of 96.5% when compared to the Virtualizer.

Following the imaging of the multi-point scatter target, imaging of a 1 cm resolution target is performed. Similar to the point scatter target, the least-squares technique is used for image reconstruction (5 iterations). The Virtualizer and FAMI reconstructed images of the resolution target are shown in Fig. 6.

Analyzing Fig. 6, it can be seen that both the Virtualizer and the FAMI reconstruct a clear outline of the resolution target. While the Virtualizer reconstruction takes 9.21 s, the FAMI completes the reconstruction in 0.28 s, 97% faster in

TABLE 3. Summary of timing of algorithms for reconstruction of 2D targets (least-squares reconstruction, 5 iterations).

Target	Virtualizer	FAMI
Point Scatter	5.71 s	0.2 s
Resolution Target	9.21 s	0.28 s

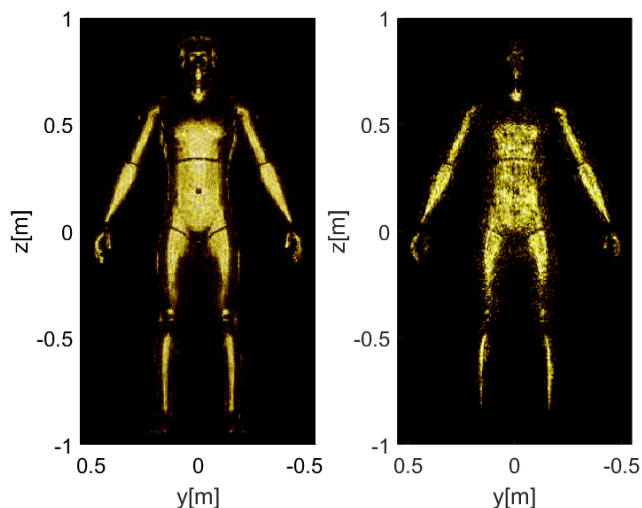**TABLE 4.** Summary of timing of algorithms for reconstruction of the human form target.

Calculation Step	Virtualizer	FAMI
Adjoint Reconstruction	7.2 s	0.28 s
Least-Squares Reconstruction (5 iterations)	121.7 s	2.6 s
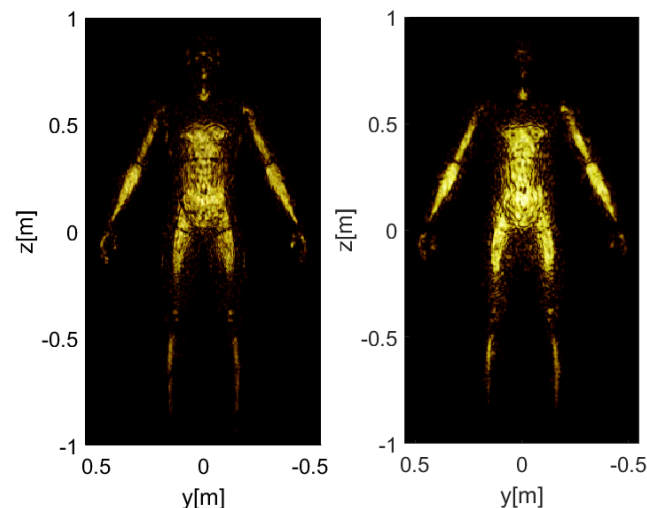
FIGURE 7. A comparison of the matched-filter reconstructions of the Virtualizer (left) and the FAMI reconstruction (right). The dynamic range for plotting is 20 dB.

comparison to the Virtualizer. A comparison between the Virtualizer and FAMI reconstruction times for the multi-point scatter and 1 cm resolution targets is given in Table 3. It should be noted here that both the multi-point scatter target in Fig. 5 and the resolution target in Fig. 6 are 2D planar targets defined in the cross-range plane. As a more realistic and complicated target, finally, we image an object of human form, which extends in both the range and cross-range planes (3D).

For this analysis, different from the 2D targets, two reconstruction methods are used; matched-filter (adjoint operation) and least-squares (adjoint and forward operations). The reconstruction of the human form target using just the adjoint operation is shown in Fig. 7. The two reconstructions look very similar, however, FAMI required 0.28 s rather than 7.2 s to perform the adjoint operation when compared to the Virtualizer. The least-squares solution (5 iterations) is demonstrated in Fig. 8. FAMI completes the reconstruction in 2.6 s, while the Virtualizer completes the task in 121.7 s, so that FAMI requires 2.1% of the time. A summary of timings is given in Table 4.

VI. CONCLUSION

FAMI is a multistatic radar imaging algorithm that is able to adapt to large separations between transmitters and receivers and highly irregular radiation patterns. It is readily parallelizable, and adaptable to GPGPU processing as it can utilize built-in features such as texture mapping to accelerate computation. It is nearly capable of real-time video-rate processing, and to our knowledge, there are no other suitable algorithms for MIMO radar processing in real-time when using complex radiation patterns or irregularly spaced antennas. While fast data acquisition is possible using electronic frequency scanning, without a suitable rapid reconstruction method, the goal of real-time radars for security checkpoint screening or navigation can not be realized. Methods such as FAMI may make metamaterial-based antenna imagers sufficiently fast to become integral parts of the nascent ubiquitous millimeter-wave radar systems.

ACKNOWLEDGMENTS

REFERENCES

[1] J. Li and P. Stoica, *MIMO Radar Signal Processing*. Hoboken, NJ, USA: Wiley, 2009.

[2] V. S. Chernyak, *Fundamentals of Multisite Radar Systems: Multistatic Radars and Multistatic Radar Systems*. Amsterdam, The Netherlands: Gordon and Breach, 1998.

[3] E. Hanle, "Survey of bistatic and multistatic radar," *IEE Proc. F Commun., Radar Signal Process.*, vol. 133, no. 7, pp. 587–595, Dec. 1986.

[4] D. L. Marks, J. Gollub, and D. R. Smith, "Spatially resolving antenna arrays using frequency diversity," *J. Opt. Soc. Amer. A, Opt. Image Sci.*, vol. 33, no. 5, pp. 899–912, 2016.

[5] A. J. Devaney, *Mathematical Foundations of Imaging, Tomography and Wavefield Inversion*. Cambridge, U.K.: Cambridge, 2012.

[6] R. H. Stolt, "Migration by Fourier transform," *Geophysics*, vol. 43, no. 1, pp. 23–48, 1978.

[7] J. Gazdag, "Wave equation migration with the phase-shift method," *Geophysics*, vol. 43, no. 7, pp. 1342–1351, 1978.

[8] D. Ristow and T. Ruhl, "Fourier finite-difference migration," *Geophysics*, vol. 59, no. 12, pp. 1882–1893, 1994.

[9] P. L. Stoffa, J. T. Fokkema, R. M. de Luna Freire, and W. P. Kessinger, "Split-step Fourier migration," *Geophysics*, vol. 55, no. 4, pp. 410–421, 1990.

[10] R. Barrett *et al.*, *Templates for the Solution of Linear Systems: Building Blocks for Iterative Methods*, vol. 43. Cambridge, U.K.: Cambridge Univ. Press, 1994.

[11] G. Lipworth *et al.*, "Comprehensive simulation platform for a metamaterial imaging system," *Appl. Opt.*, vol. 54, no. 31, pp. 9343–9353, 2015.

[12] O. Yurduseven, J. N. Gollub, A. Rose, D. L. Marks, and D. R. Smith, "Design and simulation of a frequency-diverse aperture for imaging of human-scale targets," *IEEE Access*, vol. 4, pp. 5436–5451, 2016.

[13] N. J. Willis, "Bistatic radar," in *Radar Handbook*, M. I. Skolnik, Ed. New York, NY, USA: McGraw Hill, 1990, ch. 25, pp. 25-1–25-35.

[14] N. J. Willis, *Bistatic Radar*, vol. 2. Raleigh, NC, USA: SciTech Publishing, 2005.

[15] D. D.'Aria, A. M. Guarnieri, and F. Rocca, "Focusing bistatic synthetic aperture radar using dip move out," *IEEE Trans. Geosci. Remote Sens.*, vol. 42, no. 7, pp. 1362–1376, Jul. 2004.

[16] O. Loffeld, H. Nies, V. Peters, and S. Knedlik, "Models and useful relations for bistatic SAR processing," *IEEE Trans. Geosci. Remote Sens.*, vol. 42, no. 10, pp. 2031–2038, Oct. 2004.

[17] G. Krieger, N. Gebert, and A. Moreira, "Unambiguous SAR signal reconstruction from nonuniform displaced phase center sampling," *IEEE Geosci. Remote Sens. Lett.*, vol. 1, no. 4, pp. 260–264, Oct. 2004.

[18] B. Liu, T. Wang, Q. Wu, and Z. Bao, "Bistatic SAR data focusing using an omega-k algorithm based on method of series reversion," *IEEE Trans. Geosci. Remote Sens.*, vol. 47, no. 8, pp. 2899–2912, Aug. 2009.

[19] V. Giroux, H. Cantalloube, and F. Daout, "An omega-k algorithm for SAR bistatic systems," in *Proc. IGARSS*, vol. 5. Jul. 2005, pp. 1060–1063.

[20] B. Sun, J. Lopez, and Z. Qiao, "Image reconstruction and compressive sensing in MIMO radar," *Proc. SPIE*, vol. 9077, p. 90770O, Jun. 2014 doi:10.1117/12.2051275.

[21] J. Lopez and Z. Qiao, "Array geometries, signal type, and sampling conditions for the application of compressed sensing in MIMO radar," *Proc. SPIE*, vol. 8717, p. 871702, May 2013, doi:10.1117/12.2016296.

[22] J. H. G. Ender, "On compressive sensing applied to radar," *Signal Process.*, vol. 90, no. 5, pp. 1402–1414, 2009.

[23] V. M. Patel, G. R. Easley, D. M. Healy, Jr., and R. Chellappa, "Compressed synthetic aperture radar," *IEEE J. Sel. Topics Signal Process.*, vol. 4, no. 2, pp. 244–254, Apr. 2010.

[24] M. T. Alonso, P. Lopez-Dekker, and J. J. Mallorqui, "A novel strategy for radar imaging based on compressive sensing," *IEEE Trans. Geosci. Remote Sens.*, vol. 48, no. 12, pp. 4285–4295, Dec. 2010.

[25] M. C. Shastry, R. M. Narayanan, and M. Rangaswamy, "Compressive radar imaging using white stochastic waveforms," in *Proc. Waveform Diversity Design Conf. (WDD) Int.*, Aug. 2010, pp. 000090–000094.

[26] T. D. R. Hartley, A. R. Fasih, C. A. Berdanier, F. Ozguner, and U. V. Catalyurek, "Investigating the use of GPU-accelerated nodes for SAR image formation," in *Proc. IEEE Int. Conf. Cluster Comput. Workshops*, Sep. 2009, pp. 1–8.

[27] A. Fasih and T. Hartley, "GPU-accelerated synthetic aperture radar backprojection in CUDA," in *Proc. IEEE Radar Conf.*, May 2010, pp. 1408–1413.

[28] J. Panetta *et al.*, "Accelerating Kirchhoff migration by CPU and GPU cooperation," in *Proc. SBAC-PAD*, 2009, pp. 26–32.

[29] X. Ning, C. Yeh, B. Zhou, W. Gao, and J. Yang, "Multiple-GPU accelerated range-Doppler algorithm for synthetic aperture radar imaging," in *Proc. IEEE RadarCon (RADAR)*, May 2011, pp. 698–701.

[30] P. Xueming, W. Yanping, T. Weixian, H. Wen, and W. Yirong, "GPU acceleration of 3D SAR imaging using range migration techniques," in *Proc. 3rd Int. Asia–Pacific Conf. Synth. Aperture Radar (APSAR)*, Sep. 2011, pp. 1–4.

[31] C. Clemente, M. di Bisceglie, M. di Santo, N. Ranaldo, and M. Spinelli, "Processing of synthetic aperture radar data with GPGPU," in *Proc. IEEE Workshop Signal Process. Syst.*, Oct. 2009, pp. 309–314.

[32] B. Liu, K. Wang, X. Liu, and W. Yu, "An efficient signal processor of synthetic aperture radar based on GPU," in *Proc. 8th Eur. Conf. Synth. Aperture Radar (EUSAR)*, Jun. 2010, pp. 1–4.

[33] B. Liu, K. Wang, X. Liu, and W. Yu, "Range cell migration correction using texture mapping on GPU," in *Proc. IEEE 10th Int. Conf. Signal Process.*, Oct. 2010, pp. 2172–2175.

[34] J. Hunt *et al.*, "Metamaterial apertures for computational imaging," *Science*, vol. 339, no. 6117, pp. 310–313, 2012.

[35] G. Lipworth *et al.*, "Metamaterial apertures for coherent computational imaging on the physical layer," *J. Opt. Soc. Amer. A*, vol. 30, no. 8, pp. 1603–1612, 2013.

[36] M. Slaney, A. C. Kak, and L. E. Larsen, "Limitations of imaging with first-order diffraction tomography," *IEEE Trans. Microw. Theory Techn.*, vol. 32, no. 8, pp. 860–874, Aug. 1984.

[37] L. Mandel and E. Wolf, *Optical Coherence and Quantum Optics*. New York, NY, USA: SIAM, 1995.

[38] J. N. Gollub *et al.*, "Large metasurface aperture for millimeter wave computational imaging at the human-scale," *Sci. Rep.*, vol. 7, p. 42650, 2017.

[39] O. Yurduseven, J. N. Gollub, K. P. Trofatter, D. L. Marks, A. Rose, and D. R. Smith, "Software calibration of a frequency-diverse, multistatic, computational imaging system," *IEEE Access*, vol. 4, pp. 2488–2497, 2016.

DANIEL L. MARKS was born in Chicago, IL, USA, in 1973. He received the B.S., M.S., and Ph.D. degrees from the University of Illinois at Urbana–Champaign in 1995, 1998, and 2001, respectively. From 2002 to 2008, he was a Research Scientist with the Biophotonics Laboratory, University of Illinois at Urbana–Champaign. In 2009, he joined Duke University, where he is currently an Associate Research Professor with the Department of Electrical and Computer Engineering. He has authored 85 research articles, holds 17 patents, and has been an Editor of *Applied Optics*. His research interests include optics, optical design, computational imaging, millimeter-wave and terahertz imaging, metamaterials and synthetic electromagnetic structures.

The theme of his research is the joint design of sensing systems with corresponding computational methods.

He was with the University of Illinois, as a Co-Inventor of Interferometric Synthetic Aperture Microscopy, a method of applying synthetic aperture radar reconstruction methods to 3-D biological imaging and nonlinear interferometric vibrational imaging, a method of high resolution Raman spectroscopy using femtosecond radiation.

He was the Lead Optical Designer for the DARPA AWARE Wide FOV Project, where he designed the optics for cameras varying from 0.3 to 8.5 gigapixels, and also designed and implemented GPU-based real-time gigapixel-scale stitching algorithms. He also designed a superbroadband and compact short and long wave infrared weapon scope for the DARPA Dual Use Detector Ensemble Project. He is currently a member of the Duke Center for Metamaterials and Integrated Plasmonics Metamaterial Millimeter-Wave Imager project, for which he develops antennas, algorithms, and GPU computational methods.

OKAN YURDUSEVEN (S'09–M'11–SM'16) received the B.Sc. and M.Sc. degrees in electrical engineering from Yildiz Technical University, Istanbul, Turkey, in 2009 and 2011, respectively, and the Ph.D. degree in electrical engineering from Northumbria University, Newcastle upon Tyne, U.K., in 2014.

From 2009 to 2011, he was a Research Assistant with the Department of Electrical and Electronic Engineering, Marmara University, Istanbul, Turkey. From 2011 to 2014, he was a Lecturer (part-time) with the Faculty of Engineering and Environment, Northumbria University. Since 2014, he has been a Post-Doctoral Associate with the Center for Metamaterials and Integrated Plasmonics, Department of Electrical and Computer Engineering, Duke University, working in collaboration with the U.S. Department of Homeland Security.

He has authored over 70 technical journal and conference papers, and two provisional patents. His research interests include microwave and millimeter-wave imaging, multiple-input-multiple-output radar imaging, wireless power transfer, antennas and propagation, antenna measurement techniques, and metamaterials. He has organized and chaired several special sessions within these fields at various international conferences, including the IEEE International Symposium on Antennas and Propagation and European Conference on Antennas and Propagation.

Dr . Yurduseven is a member of the European Association on Antennas and Propagation. He was a recipient of the Academic Excellence Award from the Association of British–Turkish Academics, London, in 2013. He received the best paper award at the Mediterranean Microwave Symposium in 2012 and the Travel Award from the Institution of Engineering and Technology. He has recently been nominated for the Outstanding Postdoc Award at Duke University. He serves as a Reviewer of the IEEE Transactions on Antennas and Propagation, the IEEE Transactions on Microwave Theory and Techniques, the IEEE Antennas and Wireless Propagation Letters, Progress in Electromagnetics Research, and Applied Physics B.

DAVID R. SMITH (M'98) received the Ph.D. degree in physics from the University of California at San Diego (UCSD). He is currently the Department Chair and the James B. Duke Professor of Electrical and Computer Engineering with Duke University and also the Director of the Center for Metamaterials and Integrated Plasmonics. He also holds the positions of adjunct professor at the Physics Department, UCSD, affiliate faculty at the Electrical and Computer Engineering Department, University of Washington, and visiting professor of Physics at the Imperial College, U.K. His research interests include the theory, simulation and characterization of unique electromagnetic structures, including photonic crystals and metamaterials, and applications of such materials.

He and his colleagues demonstrated the first left-handed (or negative index) metamaterial at microwave frequencies at UCSD in 2000. He has over 200 publications on matematerials and plasmonics, and was selected by ISI-Reuters as a Citation Laureate in 2009 for the most number of highly cited papers in the field of Physics over the last decade. He was once again recognized as one of the Highly Cited Researches 2014 by ISI-Reuters in the category of Physics.

Dr. Smith was elected a member of The Electromagnetics Academy in 2002. In 2005, he was part of a five member team that received the Descartes Research Prize, by the European Union, for their contributions to metamaterials and other novel electromagnetic materials. He also received the Stansell Research Award from the Pratt School of Engineering, Duke University, in 2005. In 2006, he was selected as one of the Scientific American 50, a group recognized by the editors of Scientific American for achievements in science, technology and policy. His work has twice appeared on the cover of Physics Today, and twice has been selected as one of the Top Ten Breakthroughs of the year by Science Magazine. In 2013, he was a co-recipient of the James C. McGroddy Prize for New Materials, by the American Physical Society.

In 2006, he along with colleague Sir John Pendry, suggested metamaterials could be used to design an electromagnetic cloak, introducing the new design tool of transformation optics. In 2013, he was asked to write an op-ed piece for the New York Times on cloaking research.

In 2013, he served as the Founding and Acting Director of the Metamaterials Commercialization Center, a unit within the Intellectual Ventures, Bellevue, WA, dedicated to commercializing metamaterials concepts. MCC has thus far produced three spin out companies, such as Kymeta Corporation, Redmond, WA, Evolv Technologies, Waltham, MA, and Echodyne, Bellevue, WA. He serves on the Advisory Board of Kymeta, which targets metamaterial-based antennas for satellite communications, and also a Co-Founder of Evolv Technologies, which targets metamaterial apertures for security screening applications, and Echodyne, which is seeking to apply metamaterial apertures to radar applications.

● ● ●